Alessandro Masci
Department of Electrical, Electronic and
Information Engineering (DEI),
University of Bologna,
Bologna 40126, Italy
e-mail: alessandro.masci4@unibo.it

Martino Alessandrini
Department of Electrical, Electronic and
Information Engineering (DEI),
University of Bologna,
Bologna 40126, Italy

Davide Forti
Chair of Modelling and
Scientific Computing (CMCS),
École Polytechnique Fédérale de Lausanne,
Lausanne CH-1015, Switzerland

Filippo Menghini
Chair of Modelling and
Scientific Computing (CMCS),
École Polytechnique Fédérale de Lausanne,
Lausanne CH-1015, Switzerland

Luca Dedé
Mathematics Department Politecnico di Milano,
MOX,
Milano 20133, Italy
e-mail: luca.dede@polimi.it

Corrado Tomasi
Santa Maria delle Croci Hospital,
Ravenna 48121, Italy
e-mail: c.tomasi@ausl.ra.it

Alfio Quarteroni
Professor
Mathematics Department Politecnico di Milano,
MOX,
Milano 20133, Italy
e-mail: alfio.quarteroni@polimi.it

Cristiana Corsi
Department of Electrical, Electronic and
Information Engineering (DEI),
University of Bologna,
Bologna 40126, Italy
e-mail: cristiana.corsi3@unibo.it

A Proof of Concept for Computational Fluid Dynamic Analysis of the Left Atrium in Atrial Fibrillation on a Patient-Specific Basis

Atrial fibrillation (AF) is associated with a fivefold increase in the risk of cerebrovascular events, being responsible of 15–18% of all strokes. The morphological and functional remodeling of the left atrium (LA) caused by AF favors blood stasis and, consequently, stroke risk. In this context, several clinical studies suggest that the stroke risk stratification could be improved by using hemodynamic information on the LA and the left atrial appendage (LAA). The goal of this study was to develop a personalized computational fluid dynamics (CFD) model of the LA which could clarify the hemodynamic implications of AF on a patient-specific basis. In this paper, we present the developed model and its application to two AF patients as a preliminary advancement toward an optimized stroke risk stratification pipeline. [DOI: 10.1115/1.4044583]

1 Introduction

Atrial fibrillation (AF) is the most common form of arrhythmia worldwide. It has been estimated that the prevalence of AF in the U.S. is about 2.2×10^6 including paroxysmal or persistent AF [1]. Similarly, the ATRIA study [2] observed a prevalence of AF of 0.95% in the North American general population and congruent data with respect to this study have also been obtained in the UK. There are about 160,000 new AF cases each year only in the U.S. and in the European countries. It is known that AF is an independent risk factor for stroke, and it is associated with a fourfold to fivefold increased risk of cerebrovascular events, being responsible of 15–18% of all strokes [3]. Indexes routinely used in clinical practice to stratify stroke risk, such us the CHA_2DS_2-VASc score [4], are based on empirical information without considering specific hemodynamic implications of AF which might improve the predictive power of such scores [5]. AF leads to left atrium (LA) structural remodeling [6], which consists of a progressive LA enlargement [7] and in left atrium appendage (LAA) elongation [8] and, consequently, to an alteration of the mechanical function, which causes a chaotic and strongly reduced contractile activity of LA cells. These changes could modify the physiological hemodynamics within the LA fostering blood stasis, clot formation, and embolism.

Computational fluid dynamics (CFD) represents a valuable non-invasive approach to determine and assess physically meaningful parameters and indicators in a complex fluid dynamics system, such as the cardiac blood flowrates, vorticity, turbulent kinetic energy, etc. CFD modeling of the LA in AF has not been faced
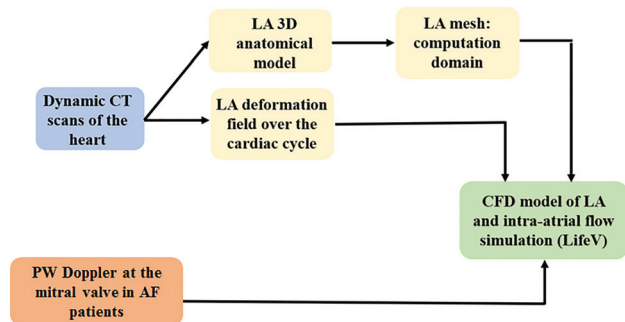
Fig. 1 Flowchart of the steps developed in this study to derive the CFD model (green box): patient-specific data (light blue boxes) processed to derive the LA anatomical and deformation model (yellow boxes) are the inputs for the final personalized CFD model. The orange box indicates input to the model using values from the literature that are not patient-specific.

exhaustively considering the relevance of the potential clinical impact. Most of the modeling studies are focused on ventricular fluid-dynamics [9–11]. The first model developed for the LA, was proposed by Zhang and Gay [12]. No patient-specific information related to chamber morphology and motion was included in the model. Koizumi et al. [13] used a real LA geometry from a healthy volunteer; the LA motion model was defined considering the location of the mitral valve (MV) annulus in the magnetic resonance images and some reference anatomical points manually extracted on the left side of the mitral annulus. This approach implies a simplification when the motion of the LA wall is considered. More in detail, LA movement of the lower part of the LA wall was computed with the assumption of a simple compression/extension in one direction and linearly increasing the compression rate toward the MV on the other direction; the movement of the upper part of the LA was fixed. In addition, boundary conditions were defined considering fixed pressure values taken from the literature. In Ref. [14], García-Isla et al. evaluated the stroke risk associated with four different LA/LAA morphologies by the CFD simulations and derived hemodynamics parameters. Yet, the simulations considered a fixed geometry and therefore could not account for the effect of wall motion on blood dynamics. A computational study in an idealized LA geometry was performed in Ref. [15] to investigate the blood flow behavior and properties, namely, transition to turbulence—in physiological conditions. Otani et al. [16] presented the first framework for personalized blood flow analysis in the LA based on computed tomography (CT) imaging. The proposed model also included the left ventricle during ventricular diastole and the pulmonary veins (PVs) were modeled as cylinders.

In our previous preliminary study [17], we proposed a pipeline for the computation of fluid dynamics of the LA in AF. In this study, we tested the previously developed approach in AF patients, in both sinus rhythm (SR) and AF conditions, for a comprehensive evaluation of hemodynamic implications of AF episodes in both LA chamber and LAA, including velocity and vortex structures.

2 Methods

A schematic depiction of the workflow designed and developed in this study is shown in Fig. 1. Briefly, our personalization pipeline involved using the dynamic CT imaging to reconstruct the moving patient-specific three-dimensional (3D) atrial anatomy over the cardiac cycle (Fig. 1, light blue boxes). Processed patient data were then provided as input to the CFD solver (Fig. 1, light yellow boxes). A representative MV flow rate from intracardiac pulsed wave (PW) Doppler in AF patients was used to set boundary conditions for the CFD simulations (Fig. 1, orange box) [13]. The workflow was applied to two persistent AF patients [18].

Computed tomography dynamic acquisition was performed in sinus rhythm using a 64-slice multidetector CT scanner (Philips Brilliance 64 CT scanner) in each of the two patients enrolled in the study. The study was approved by the Ethics IRST, IRCCS AVR Committee (CEIIAV n. 1456 prot. 6076/2015 I.5/220). Informed consent was obtained from the subjects. Volumetric CT images were reconstructed for a total of ten phases from ventricular end-diastole (from 0%RR to 90%RR, where RR indicates the interval between two consecutive electrocardiographic R wave peaks). Each reconstructed CT volume was $512 \times 512 \times 180$ pixels. The voxel resolution was not isotropic: in-plane resolution was 0.39 mm, and through-plane resolution was 1 mm, resulting in a voxel size of $0.39 \times 0.39 \times 1$ mm^3.

For the MV flowrate computation, we multiplied the MV Doppler velocity by the MV cross-sectional area.

2.1 Definition of the Anatomical Model of the Left Atrium. The LA was detected by processing the first volume of the CT dynamic acquisition. A volume of interest including the LA was manually selected. The LA was detected in each image of the volume of interest, and the 3D LA was then reconstructed. Two-dimensional segmentation was automatically performed applying an adaptive thresholding approach considering the histogram of each CT image. Based on the acquisition protocol, we hypothesized that the peak of the histogram corresponds to the gray level intensity of the LA chamber (int$_{max}$).

This peak was automatically detected and, based on this value, we fixed two thresholds defined as in the following:

$$\text{th}_{\text{down}} = \text{int}_{\text{max}} - q \cdot \text{int}_{\text{max}} \tag{1}$$

$$\text{th}_{\text{up}} = \text{int}_{\text{max}} + q \cdot \text{int}_{\text{max}} \tag{2}$$

where the constant q is a percentage value: in particular, if int$_{max}$ was in the higher tertile of intensity values, q was defined as 5%; otherwise q was set to 3%. By selecting the gray level values between th$_{\text{down}}$ and th$_{\text{up}}$, a rough detection of the LA was obtained. Further processing was designed to improve LA segmentation accuracy. We first applied some morphological operators to disconnect regions and regularize the contours. Then, for each slice the region with the biggest area was selected. Since in the top slices of the axial acquisition the LAA might be disconnected from the LA chamber, we automatically detected these slices in which the two biggest connected regions corresponding to the LA and the LAA were selected. Finally, to refine the segmentation obtained in the previous steps, we applied a curvature motion to regularize the LA contour in each slice. Figure 2 shows the result of the LA segmentation in one patient, in three of the most challenging axial slices in which the LA and the LAA (top and mid rows) and the left ventricle (bottom row) are visible. Once applied all the steps described previously, the 3D anatomy was then obtained by stacking the two-dimensional segmentations. This algorithm was implemented in MATLAB R2016a [19]. In addition, to comply with the requirement of providing a smooth geometrical representation of the computational domain for the CFD simulation, our 3D anatomical model was (i) further filtered by applying a Laplacian smoothing using MESHLAB software [20]; and (ii) five cut planes were applied to the four PVs and the MV to define inflows and outflow boundary subsets of the anatomical model for the CFD simulation. This final anatomical model was used as the input for the labeling and volume mesh generation algorithm: for this step, the vascular modeling toolkit (VMTK) library was employed [21]. An example of the final result of the LA mesh in one patient is shown in Fig. 3.

2.2 Computation of the Left Atrium Deformation Over the Cardiac Cycle. The deformation of the LA throughout the time instants of the cardiac cycle was computed by applying a 3D nonrigid image registration step of the CT volumes. In this way,
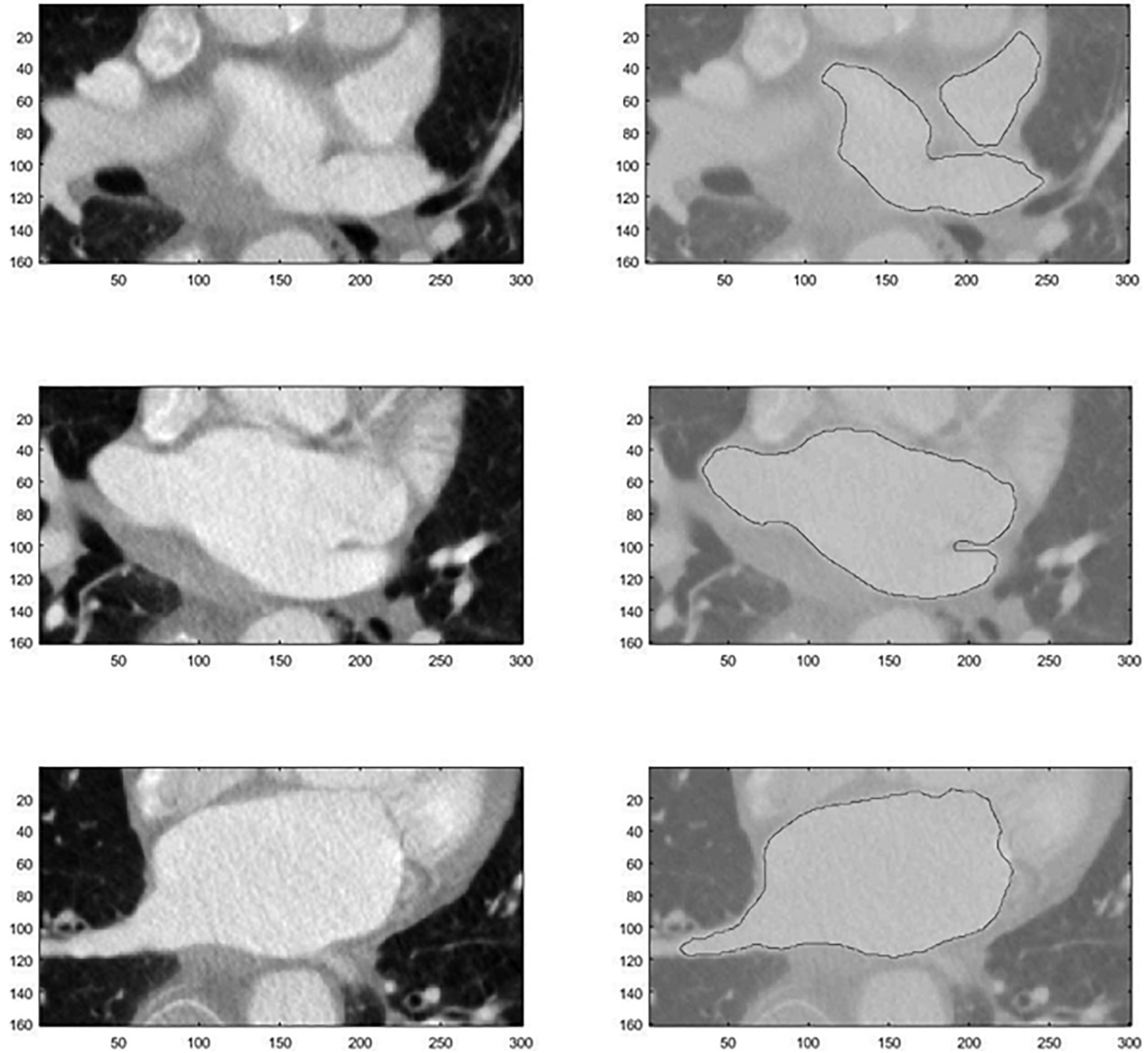
Fig. 2   Result of the LA segmentation in three axial slices at different levels of the LA chamber: CT images are shown in the left column and the corresponding segmentation is shown in the right column. Note that in the first row the segmentation of the LAA is also visible.
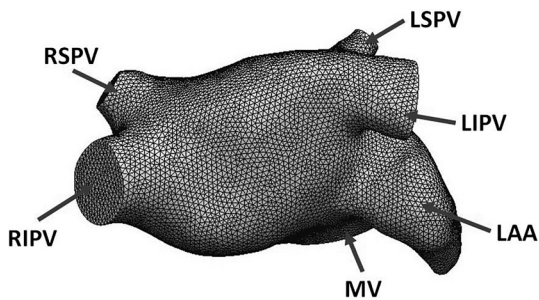

Fig. 3   Representation of the LA mesh in one patient (RIPV, right inferior pulmonary vein; RSPV, right superior pulmonary vein; LSPV, left superior pulmonary vein; LIPV, left inferior pulmonary vein; LAA, left atrial appendage; and MV, mitral valve)

we computed the displacement $\mathbf{s}_{i \to i+1}(\mathbf{x})$ between two successive CT volumes $\mathrm{Im}_i(\mathbf{x})$ and $\mathrm{Im}_{i+1}(\mathbf{x})$. Before the application of the nonrigid registration step, we decided to perform an affine transformation. Afterward, the result obtained was combined with the nonrigid transformation based on *B-spline* [22] model. It was defined as

$$\mathbf{T}(\mathbf{x}) = \mathbf{x} + \sum_{\mathbf{x}_k \in \mathcal{N}_x} \mathbf{p}_k \boldsymbol{\beta}^3 \left(\frac{\mathbf{x} - \mathbf{x}_k}{\boldsymbol{\sigma}} \right) \qquad (3)$$

with $\mathbf{x}_k$ the control points, $\boldsymbol{\beta}^3(\mathbf{x})$ the cubic multidimensional B-spline polynomial [22], $\mathbf{p}_k$ the B-spline coefficient vectors (the control point displacements), $\boldsymbol{\sigma}$ represents the spacing of the B-spline control points, and $\mathcal{N}_x$ the set of all control points within the compact support of the B-spline at $\mathbf{x}$. The control points $\mathbf{x}_k$ were defined on a regular grid, overlaid on the fixed image. The control point grid was defined by the amount of space between the control points $\boldsymbol{\sigma} = (\sigma_1, \dots, \sigma_{d_{\mathrm{imm}}})$, which could be different for each direction.

The parameters in Eq. (3) were chosen for optimizing tracking quality as assessed visually. Moreover, we employed the mean square difference as the image registration measure similarity.

Following this step, the global displacement of a general CT volume at time i with respect to the reference volume (time 0) was computed by increasing the successive interframe displacements: $\mathbf{s}_{i \to 0}(\mathbf{x}) = \mathbf{s}_{i \to n-1}(\mathbf{x}) \circ \mathbf{s}_{i-1 \to 0}(\mathbf{x})$, with $\mathbf{s}_{0 \to 0}(\mathbf{x}) = \mathbf{0}$. Therefore, considering $\mathbf{x}_0$ the position of a mesh vertex at time 0, the new position $\mathbf{x}_i$ at time of the position i was calculated in this way $\mathbf{x}_i = \mathbf{x}_0 + \mathbf{s}_{n \to 0}(\mathbf{x}_0)$.

The motion field was then used to propagate the LA computational domain on the entire cardiac cycle and to simulate LA motion in SR condition. Unfortunately, the CT scanner available at the hospital that was involved in this study did not allow time-resolved images during AF episodes. LA motion in AF is defined as an irregular, disorganized, very rapid, and strongly reduced contraction. In previous studies [14,23], LA walls in AF were simulated rigid replicating the extreme condition of chronic AF when atrial contraction is not possible anymore. In our study, to simulate conditions preceding chronic AF (paroxysmal and persistent AF conditions), we modeled atrial contraction by employing a random displacement applied independently to each vertex of the anatomical LA model and consisting in a sinusoidal function at a frequency of 4 Hz multiplied by a random factor from an uniform probability density function from 0 to 1. The contraction frequency was defined considering the typical frequency of atrial fibrillatory episodes. Moreover, the sinusoidal wave was modulated by a small amplitude (0.1 mm) to mimic the reduced contraction. This also allowed to avoid numerical issues arising from an excessive worsening of the mesh quality. Considering this contraction model, in our two patients in persistent AF, LA volume variation throughout the cardiac cycle was very low (1–2%), implying no strong variation from the strategy to keep fixed the LA anatomical model over the cardiac cycle. However, we believe that the adopted model could be more realistic instead of keeping the anatomical model rigid. Moreover, to improve the temporal resolution, we applied the Fourier interpolation to the displacement field. Therefore, we were able to recover a continuous and periodic function from the discrete data available. The reconstruction of a continuous displacement function was necessary to ensure the stability of the CFD numerical model. Moreover, considering the assumed periodicity of the heartbeat, we simulated and analyzed an arbitrary number of cardiac cycles, which was necessary to avoid the unphysiological initial condition on the blood flow velocity.

2.3 The Computational Fluid Dynamic Model. The blood flow was modeled as a fluid governed by the incompressible Navier–Stokes equations written in the Arbitrary Lagrangian Eulerian frame of Refs. [11,24]. This assumption allowed to conveniently split the problem into two coupled subproblems, namely, the fluid problem, describing the fluid dynamics and the geometric problem, which attained to the motion of the computational domain to be used with the fluid problem. The latter determined the displacement of the fluid domain $\hat{\mathbf{d}}_f$ which defined the ALE map. To take into account the motion of the fluid domain $\Omega \subset \mathbb{R}^3$, we considered $\hat{\mathbf{d}}_f$ as an harmonic extension to the fluid reference domain $\hat{\Omega}$ of the displacement $\hat{\mathbf{d}}_{wall}^{(t)}$ registered at the boundary of the left atrium Ω (lateral wall, PVs, and MV), that is, for all $t \in (0, T]$

$$\begin{cases} -\Delta \hat{\mathbf{d}}_f^{(t)} = \mathbf{0} & \text{in} \quad \hat{\Omega} \\ \hat{\mathbf{d}}_f^{(t)} = \hat{\mathbf{d}}_{wall}^{(t)} & \text{on} \quad \partial\hat{\Omega} \end{cases} \quad (4)$$

Notice that $\hat{\Omega}$ was the reference domain, while Ω_t was defined as the current domain configuration. The solution of the geometry problem defined the ALE map $\mathcal{A}_t(\hat{\mathbf{x}}) = \hat{\mathbf{x}} + \hat{\mathbf{d}}_f(\hat{\mathbf{x}}, t)$ for all $\hat{\mathbf{x}} \in \Omega$ and the current fluid domain configuration. The Navier–Stokes equations for an incompressible fluid written in ALE coordinates read, for all $t > 0$

$$\begin{cases} \rho_f \frac{\partial \mathbf{u}_f}{\partial t}\bigg|_{\hat{\mathbf{x}}} + \rho_f \big((\mathbf{u}_f - \mathbf{w}) \cdot \nabla\big)\mathbf{u}_f - \nabla \cdot \boldsymbol{\sigma}_f(\mathbf{u}_f, p_f) = \mathbf{0} & \text{in} \quad \Omega_t \\ \nabla \cdot \mathbf{u}_f = 0 & \text{in} \quad \Omega_t \\ \mathbf{u}_f = \mathbf{z}_f & \text{on} \quad \Gamma_D \\ \boldsymbol{\sigma}_f \mathbf{n}_f = \mathbf{g}_f & \text{on} \quad \Gamma_N \end{cases}$$

(5)

where the initial condition is $\mathbf{u}_f = \mathbf{0}$ in Ω at the initial time $t = 0$.

$(\partial/\partial t)|_{\hat{\mathbf{x}}} = (\partial/\partial t) + \mathbf{w} \cdot \nabla$ represents the ALE derivative [25]. $\mathbf{w}(\mathbf{x}) = \big(\partial\mathcal{A}_t(\mathbf{x})/\partial t\big)$ represents the fluid velocity of the computational domain, $\mathbf{u}_f$ and p_f represent the velocity and pressure of the fluid, respectively. We denoted by ρ_f the density of the fluid, and $\boldsymbol{\sigma}_f$ is the Cauchy stress tensor for a Newtonian fluid

$$\boldsymbol{\sigma}_f(\mathbf{u}_f, p_f) = \mu\big(\nabla\mathbf{u}_f + (\nabla\mathbf{u}_f)^T\big) - p_f\mathbf{I}$$

where I is the identity tensor, μ is the dynamic viscosity of the fluid, and $\mathbf{n}_f$ is the outward normal to $\partial\Omega_t$. The functions $\mathbf{z}_f$ and $\mathbf{g}_f$ indicated the Dirichlet and Neumann data applied at the Dirichlet Γ_D and Neumann Γ_N, subsets of the boundary Ω_t, where the corresponding boundary conditions were applied.

Regarding the spatial and temporal discretization of the problem, based on the finite element (FE) method [26] and backward differentiation formulas [27], respectively, it was necessary to recall the weak formulation of the problem written in nonconservative form [28]. Let us introduce the following functional spaces:

$$U_0^f = \{\mathbf{v} = \hat{\mathbf{v}} \circ \mathcal{A}_t^{-1} | \hat{\mathbf{v}} \in [H^1(\hat{\Omega})]^3, \hat{\mathbf{v}} = \mathbf{0} \text{ on } \Gamma_D\}$$
$$U_z^f = \{\mathbf{v} = \hat{\mathbf{v}} \circ \mathcal{A}_t^{-1} | \hat{\mathbf{v}} \in [H^1(\hat{\Omega})]^3, \hat{\mathbf{v}} = \mathbf{z}_f \text{ on } \Gamma_D\}$$
$$Q^f = \{q = \hat{q} \circ \mathcal{A}_t^{-1} | \hat{q} \in [L^2(\hat{\Omega})]\}$$
$$U_{wall}^d = \{\hat{\mathbf{v}} \in [H^1(\hat{\Omega})]^3 | \mathbf{v} = \hat{\mathbf{d}}_{wall} \text{ on } \partial\Omega\}$$
$$U_0^d = \{\hat{\mathbf{v}} \in [H^1(\hat{\Omega})]^3 | \mathbf{v} = \mathbf{0} \text{ on } \partial\Omega\}$$

We recalled the notation for the Dirichlet boundary data for the fluid and domain deformation problems: $\mathbf{z}_f : \Gamma_D \to \mathbb{R}^3, \hat{\mathbf{d}}_{wall} : \partial\Omega \to \mathbb{R}^3$, respectively.

The weak formulation of the problem reads: for all $t \in (0, T]$, find $\mathbf{u}_f \in U_z^f$, $p_f \in Q^f$, $\hat{\mathbf{d}}_f \in U_{wall}^d$ satisfying

$$\int_{\Omega_t} \left(\rho_f \frac{\partial \mathbf{u}_f}{\partial t}\bigg|_{\hat{\mathbf{x}}} \cdot \mathbf{v} + \rho_f\big((\mathbf{u}_f - \mathbf{w}) \cdot \nabla\big)\mathbf{u}_f \cdot \mathbf{v}\right) d\Omega_t$$
$$+ \int_{\Omega_t} \big(\boldsymbol{\sigma}_f(\mathbf{u}_f, p_f) : \nabla\mathbf{v}\big) d\Omega_t = \int_{\Gamma_N} \mathbf{g}_f \cdot \mathbf{v} d\gamma \qquad \forall \mathbf{v} \in U_0^f$$
$$\times \int_{\Omega_t} q\nabla \cdot \mathbf{u}_f d\Omega_t = 0 \qquad \forall q \in Q^f$$
$$\times \int_{\Omega_t} \nabla_{\hat{\mathbf{x}}}\hat{\mathbf{d}}_f : \nabla_{\hat{\mathbf{x}}}\hat{\mathbf{v}}_g d\hat{\Omega} = 0 \qquad \forall \mathbf{v}_g \in U_0^d$$

where $\mathbf{w} = \big(\partial\hat{\mathbf{d}}_f/\partial t\big)$, the deformation rate of the fluid domain. For the spatial discretization, we employed the FE space $X_h^r(\Omega)$ of scalar Lagrangian basis functions of polynomial degree $r \geq 1$ over the mesh elements $K \in \mathcal{T}_h$, with $\mathcal{T}_h$ the mesh of Ω. We defined the variables $\mathbf{u}_{f_h}$ and p_{f_h} as the spatial approximations through finite element basis of degree $r = 1$ for $\mathbf{u}_f$ and p_f. We also considered finite elements of degree $r = 1 (\mathbb{P}1)$ for the spatial discretization of displacement field $\hat{\mathbf{d}}_{f_h}$. Following our choice of the finite element subspaces of the same degree $r = 1$ (the so–called finite element pair $\mathbb{P}1 - \mathbb{P}1$), we used the Variational Multiscale Stabilization-Streamline Upwind Petrov Galerkin formulation [29] for the Navier–Stokes equations to yield a stable problem in the sense of the inf–sup condition and to control numerical instabilities arising in the advection dominated regime of the flow.

Regarding the time discretization of the problem, we applied a second-order semi-implicit scheme based on backward differentiation formulas [27]. In virtue of this approach, the fully discrete semi-implicit formulation yielded a linear problem in the variables $\mathbf{u}_{f_h}^{n+1}$ and $p_{f_h}^{n+1}$ to be solved only once at each discrete time instance t_n.

2.4 Boundary Conditions Imposed to the Computational Fluid Dynamic Model. Since the inflow sections displace along the heartbeat and their sectional areas are not circular, the profile
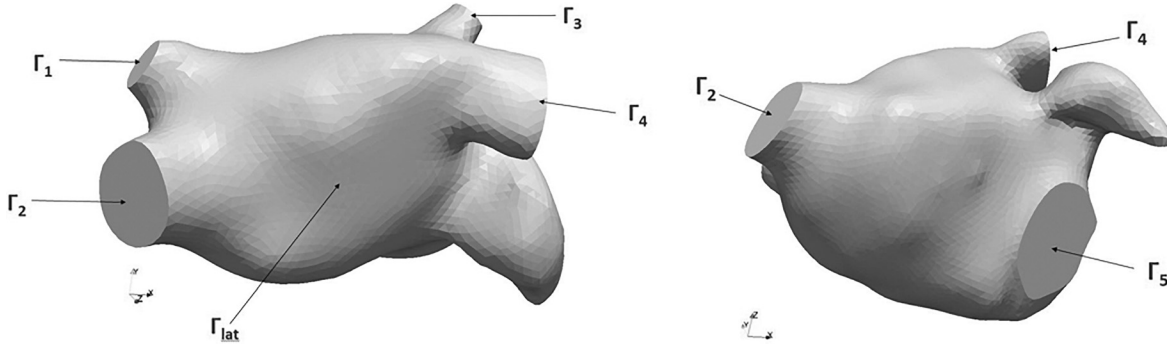
Fig. 4 Boundary regions of the anatomical model: Γ_1, Γ_2, Γ_3, and Γ_4 represent the PVs sections, Γ_5 is the MV section, and Γ_{lat} is the lateral boundary of the LA

of the inflow velocity was modeled by a pseudo-parabolic profile. To set such a profile, we solved a Laplacian problem at each pulmonary vein

$$\begin{cases} -\Delta \mathbf{u}_{BC} = 1 & \text{in} \quad \Gamma_{PV} \\ \mathbf{u}_{BC} = \mathbf{0} & \text{on} \quad \partial \Gamma_P \end{cases} \tag{6}$$

where $\mathbf{u}_{BC}$ was the solution of Eq. (6). Notice that Γ_{PV} was either Γ_1, Γ_2, Γ_3, or Γ_4 (see Fig. 4).

Through this procedure, we imposed a pseudo-parabolic flow profile at each PV to be suitably rescaled by the flowrate for $t \in (0, T]$. The pseudo-parabolic velocity profile at each PV was obtained by weighting the solution of the Laplacian problem $\mathbf{u}_{BC}$ with the current flowrate at the corresponding PV.

A representative realistic MV flowrate in AF patients in SR, Q^0, was obtained from Ref. [13]. The flowrate at each PV was computed by enforcing mass balance equation for all $t \in (0, T]$

$$Q_1^{pv} + Q_2^{pv} + Q_3^{pv} + Q_4^{pv} + Q^O + \frac{dV}{dt} = 0 \tag{7}$$

where Q_i^{pv}, $(i = 1, 2, 3, 4)$ were the flowrates of each pulmonary veins, Q^O was the flowrate at the MV section and (dV/dt) is the LA volume variation. From Eq. (7), we defined Q_{tot}^{pv}, the total flux at the PVs

$$Q_{\text{tot}}^{pv} = Q_1^{pv} + Q_2^{pv} + Q_3^{pv} + Q_4^{pv} \tag{8}$$

Afterward, to take into account the number and location of the PVs that show great variability in patients [30] and may affect LA fluid dynamics, we assigned the total flux Q_{tot}^{pv} through the four pulmonary veins with a criterion based on their sectional area

$$Q_l^{pv} = \frac{A_l}{A_{\text{tot}}} Q_{\text{tot}}^{pv}; \quad l = 1, 2, 3, 4 \tag{9}$$

where A_l is the sectional area of each PV, and A_{tot} is the sum of PVs sectional areas. In this way, for each $t \in (0, T]$, we were able to evaluate the flowrate at each PV to be applied at the computational model.

Equation (9) was then modified by including the flow due to the mesh velocity Q_l^w for each pulmonary vein during the cardiac cycle

$$Q_l^{pv} = \frac{A_l}{A_t} Q_{\text{tot}}^{pv} - Q_l^w \quad l = 1, 2, 3, 4 \tag{10}$$

In addition, for AF condition, we redefined the inflow boundary conditions by removing the A-wave from the representative MV flowrate signal Q^0 and each PV flowrate was recomputed as described before.

To limit the presence of backflows as they may give rise to numerical instabilities at the outflow boundary Γ_{out}, we considered the following natural-type boundary condition [31] with backflow penalization ($\mathbf{g}_f = \mathbf{0}$):

$$-p_f \mathbf{n} + \mu \left(\nabla \mathbf{u}_f + (\nabla \mathbf{u}_f)^{\mathrm{T}} \right) \cdot \mathbf{n} - \rho_f \left(\{\mathbf{u}_f \cdot \mathbf{n}\}_- \right) \mathbf{u}_f = \mathbf{0} \quad \text{on } \Gamma_{\text{out}} \tag{11}$$

where $\mathbf{n}$ was the outward directed unit vector normal to Γ_{out}, and $\{\mathbf{u}_f \cdot \mathbf{n}\}_-$ denoted the negative part of $\mathbf{u}_f \cdot \mathbf{n}$

$$\{\mathbf{u}_f \cdot \mathbf{n}\}_- = \begin{cases} \mathbf{u}_f \cdot \mathbf{n} & \text{if} \quad \mathbf{u}_f \cdot \mathbf{n} < \mathbf{0}, \\ \mathbf{0} & \text{if} \quad \mathbf{u}_f \cdot \mathbf{n} \geq \mathbf{0} \end{cases} \tag{12}$$

The above boundary condition was introduced to weakly penalize the reverse flow eventually induced by the backflows at Γ_{out}, which may render unstable the discrete formulation of the problem. Indeed, we observed that only if $\mathbf{u}_f \cdot \mathbf{n} < \mathbf{0}$ on Γ_{out}, the last term on the left-hand side of Eq. (11) was active; if $\mathbf{u}_f \cdot \mathbf{n} \geq \mathbf{0}$ on Γ_{out}, the outflow boundary condition reduced to the well-known stress-free condition. The LA mesh and its associated $\hat{\mathbf{d}}_{\text{wall}}$ were provided as inputs to the finite element library LifeV [32] used simulate the interatrial blood flow with the computational model.

2.5 Numerical Simulations. For each patient, we performed two numerical simulations: one corresponding to sinus rhythm (SR) and one corresponding to AF condition. As underlined in Secs. 2.2–2.4, SR and AF differ in the motion model employed: SR employed the patient-specific motion model extracted from the CT volumes. AF was instead simulated by applying independently to each mesh vertex a random displacement.

The SR and AF simulations were run for seven cardiac cycles. The results of the first three cycles were disregarded to avoid the influence of the unphysiological initial condition on the blood flow. Then, the results of the remaining cycles were phase-averaged; for example, the velocity field in every point of the domain and at a given time of the first useful heartbeat was averaged with that of the field at the corresponding point, but at times of the following heartbeats. In this manner, an average heartbeat was obtained, to account for the variability in the solution due to the nonlinearity in the Navier–Stokes equations. Steady-states were not reached, as it is intrinsic in the nature of the problem, but a phase-average solution was obtained provided that a sufficiently large number of heartbeats were involved in the averaging process. In practice, for this kind of simulation, 6–7 heartbeats suffice as shown in Refs. [10], [11], and [15]. Moreover, this kind of phase-averaging allowed a statistical study of the blood flow, in

Table 1 Number of vertices, tetrahedra of computational mesh, and associated number of degrees-of-freedom of the fluid problem for both the patients geometries

	Vertices	Tetrahedra	DOFs
Mesh 1	170,428	1,042,766	681,712
Mesh 2	131,158	798,838	524,632

terms of cycle-to-cycle variations and assessment of turbulent effects (if any).

Therefore, in the Results and Discussion section, we report the results of the averaged simulated cardiac cycle in both conditions.

3 Results and Discussion

In Table 1, we reported the information on the LA computational meshes of both patients and the respective number of degrees-of-freedom of the fluid dynamics problem. Concerning the parameters of the fluid dynamics model, the time-step was set to 0.001 s, dynamic viscosity was 0.035 poise and the density was set to 1.06 g/cm^3. For each simulated condition we evaluated and reported the most significant parameters able to describe the LA fluid dynamics including velocity and vortex structures within the LA in both patients. For a better visualization of the vortex structures, the use of the Q-criterion was preferred. It is defined as in the following:

$$Q = \frac{1}{2}(\mathbf{W}_{ij}\mathbf{W}_{ij} - \mathbf{S}_{ij}\mathbf{S}_{ij}) \qquad (13)$$

being $\mathbf{S}_{ij} = \left(\left(\partial\mathbf{u}_{f_i}/\partial\mathbf{x}_j\right) + \left(\partial\mathbf{u}_{f_j}/\partial\mathbf{x}_i\right)\right)$ and $\mathbf{W}_{ij} = \left(\left(\partial\mathbf{u}_{f_i}/\partial\mathbf{x}_j\right) - \left(\partial\mathbf{u}_{f_j}/\partial\mathbf{x}_i\right)\right)$ the symmetric and antisymmetric parts of the velocity-gradient tensor $\left(\partial\mathbf{u}_{f_i}/\partial\mathbf{x}_j\right)$. Through this quantity, we identified the connected regions where $Q > 0$, and the pressure was lower than the ambient value as the vortexes core. Finally, we focused on the fluid dynamics of the LAA: the analysis of LAA behavior is not trivial; however, it could represent an important aspect in the evaluation of the stroke risk in atrial fibrillation.

3.1 Velocity and Vorticity Analysis. An example of the computed PVs flowrates for the SR and AF simulations are shown in Fig. 5.

Focusing on the PV flowrate profile in SR condition, the S- and D-waves are clearly recognizable in the figure. The amplitude of the S-wave is strongly reduced with respect to the physiological condition [33], which is probably due to changes in the LA cell contractile activity caused by persistent AF, implying a scarce expansion of the LA during ventricular systole. Moreover, a small retrograde flow in correspondence of the late diastole phase, immediately after atrial contraction, can be easily recognized.

In Fig. 6, the LA volume variation in SR condition throughout the heartbeat is depicted. We can see that the value of the LA volume was higher (mean value throughout the cardiac cycle: 110 cm^3) than physiological values ($20-40$ cm^3) and also the maximum volume variation over the cardiac cycle was reduced 10% whereas in healthy LA the volume variation could be also 40%. These findings confirmed the anatomical and functional changes of the LA chamber due to the persistence of AF.

The simulated LA blood velocity in the two patients is displayed in Fig. 7.

In patient 1, in the first row of Fig. 7, representing blood flow velocity in correspondence of ventricular systole, we observed that flow velocity in the pulmonary veins showed an increment in the SR condition (mean value 15–20 cm/s) with respect to the AF one (mean value 5–10 cm/s). This increment was due to the atrial diastole: according to the principle of mass conservation, volume variation must be compensated by the entrance of blood flow from
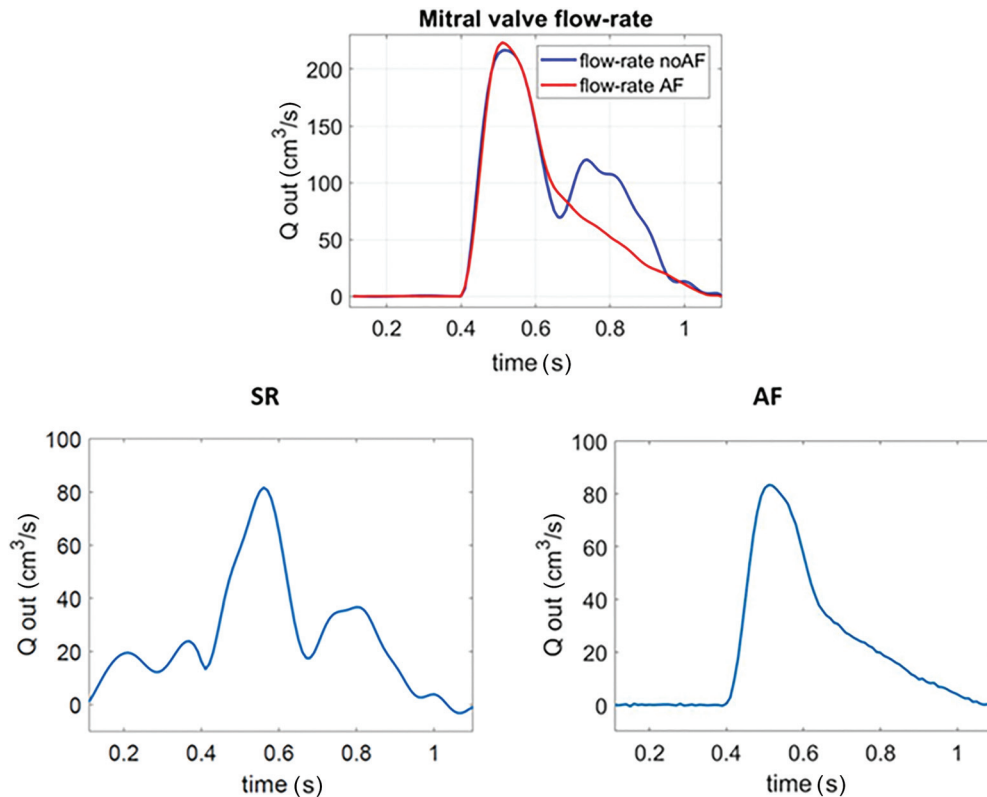
Fig. 5 Fist row: MV flowrate allows to recognize the different phases of the cardiac cycle; second row: examples of the computed PV flowrate for the SR simulation (left panel) and for the AF simulation (right panel) in one cardiac cycle
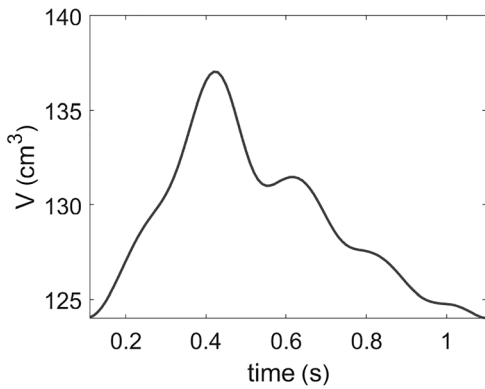
Fig. 6 LA chamber volume variation throughout the cardiac cycle in SR condition

the PVs. The magnitude of the velocity field was still relatively small; in particular, we noticed the highest velocity close to PVs was 15–20 cm/s. We also appreciated an increase of the velocity in the left-bottom part of the LA, which was probably caused by a significant expansion of this area, which retrieved blood and consequently resulted in an increase of the local fluid velocity. In AF condition, we did not appreciate an increment of velocity at PVs with respect to the SR condition: the enhanced difference was probably an effect of the random motion model that characterizes this condition. In fact, during AF, LA expansion was not evident and PV velocities remained mostly null.

During the LV filling phase, namely, in the first part of LV diastole (second row of Fig. 7) we found an appreciable increase of the velocity in proximity of the MV. In this phase, the mitral valve was open and blood rapidly flowed from the LA to the LV. Velocity at the MV reached the peak value of 65–70 cm/s. An expected increase of PV velocity was confirmed by the simulation results (mean value 40 cm/s). In this phase, we did not notice relevant differences between the two simulated conditions.

During atrial systole (third row of Fig. 7), we appreciated an important difference between the SR and AF conditions. In fact, we observed an expected increment of the blood flow velocity in proximity of the MV only in SR simulation (peak value $35 - 40$ cm/s): this difference was due to the A wave peak of the MV flow-rate, which corresponded to the atrial contraction. For the AF condition, the A wave was instead missing, and for this reason, we did not observe an increment of velocity at the MV. In fact, the velocity value remained about $20 - 25$ cm/s.

For patient 2 (see Fig. 7), as expected, we found that the velocity distribution within the LA was very similar to the ones obtained in patient 1. Since both patients suffered from persistent AF, it was not unexpected that the LA volume variation throughout the cardiac cycle in SR condition was very similar between them. We noticed that, in patient 2, velocity in proximity of the MV during the first phase of ventricular diastole reached the value of 55 cm/s, which was a lower value compared to patient 1 $(65 - 70$ cm/s), and it was probably due to the difference of the MV annulus area, larger in the second analyzed patient, thus implying a lower velocity through the outflow. Moreover, just like in patient 1, the complexity of the flow pattern within the LA was enhanced by the tridimensional representation of the velocity field.

Regarding the representation of the vortex structures within the left atrium, results are shown in Figs. 8 and 9.

Vortex dynamics was very complex during the ventricular systole (first row, Fig. 8) and the number of vortex structures was higher in SR condition than in AF. We hypothesize that the velocity distribution in the atrial vortices may favor a better "washout" effect and avoid intra-atrial blood flow stasis. For this reason, a smaller number of vortexes of the same intensity in AF condition may promote blood stasis within LA.

In correspondence of the first part of the ventricular diastole (second row, Fig. 8), vortex structures increased and were associated with high velocity values. In particular, four vortex rings were ejected from the PVs and propagated toward the center of the atrial cavity. Moreover, vortexes around the MV caused by the exit of the blood flow in this phase were visible.
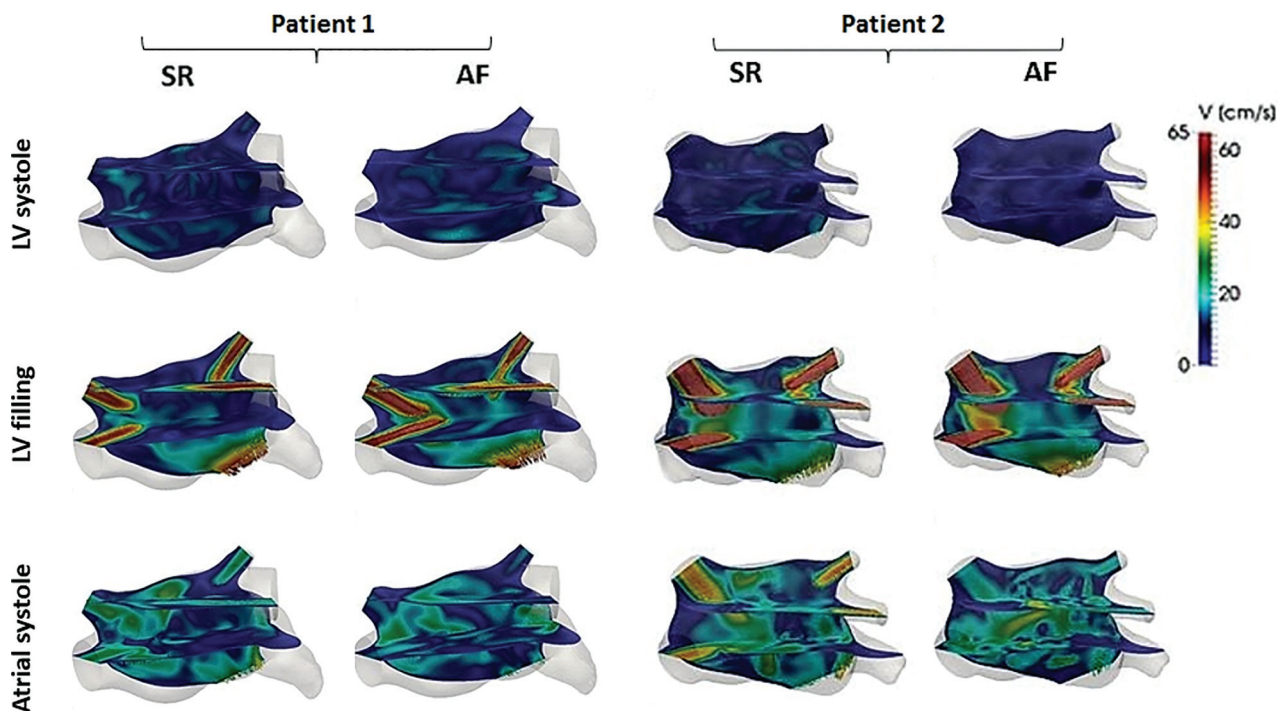

Fig. 7 Blood flow velocity distributions within the LA are shown in the two patients in SR (first/third column) and in AF (second/fourth column) at different times during the cardiac cycle: LV sistole; LV filling (*E*-wave); atrial systole (*A*-wave) in the first, second, and third row, respectively. To allow better visualization, blood flow distribution is shown in three orthogonal planes.
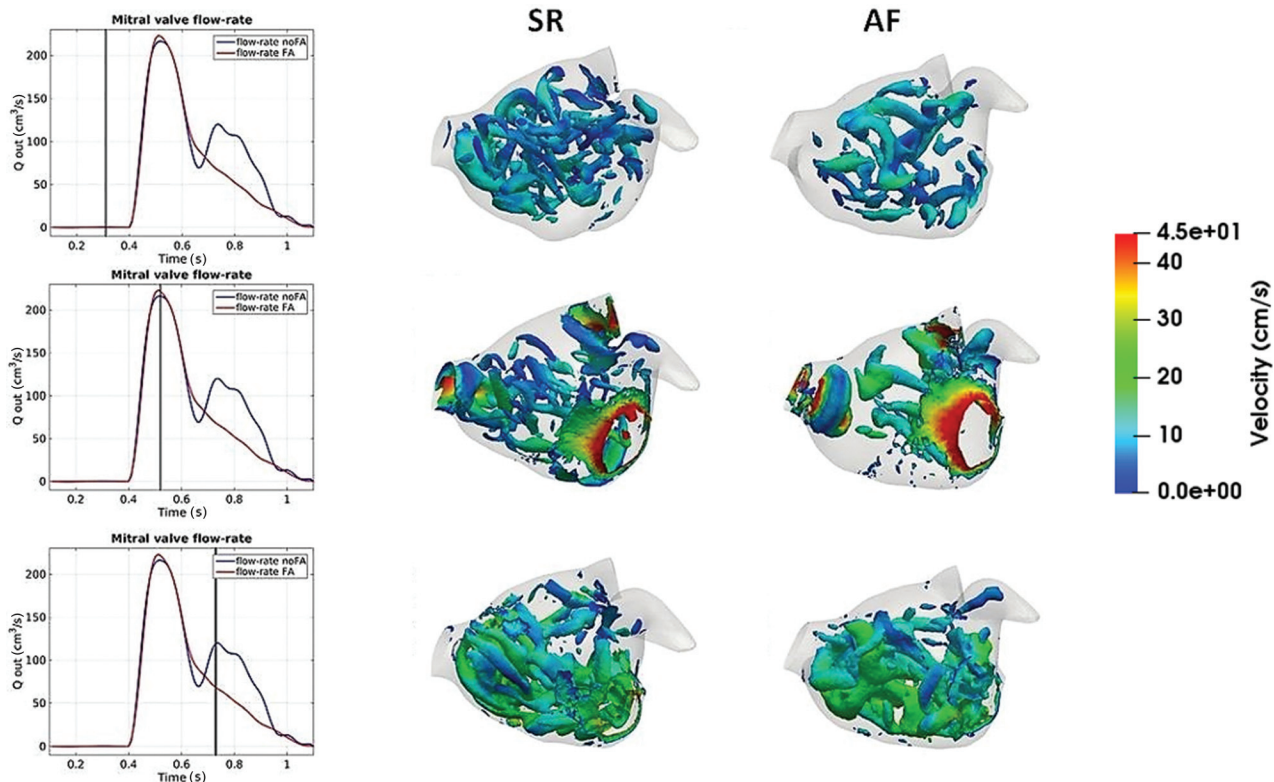
Fig. 8   Visualization of the vortexes structures within the LA in patient 1, at three instants of the cardiac cycle

During the second part of the ventricular diastole (third row, Fig. 8), the propagation of these vortex rings from the PVs brought them into direct interaction with each other and leads to a vortex breakup and consequently to a decrease of the vortex structures or dissociation into a number of small-scale vortex structures: this was due to collisions between vortexes at various inclination angles and their subsequent breakdown was due to nonuniform stretching and enhanced viscous dissipation.
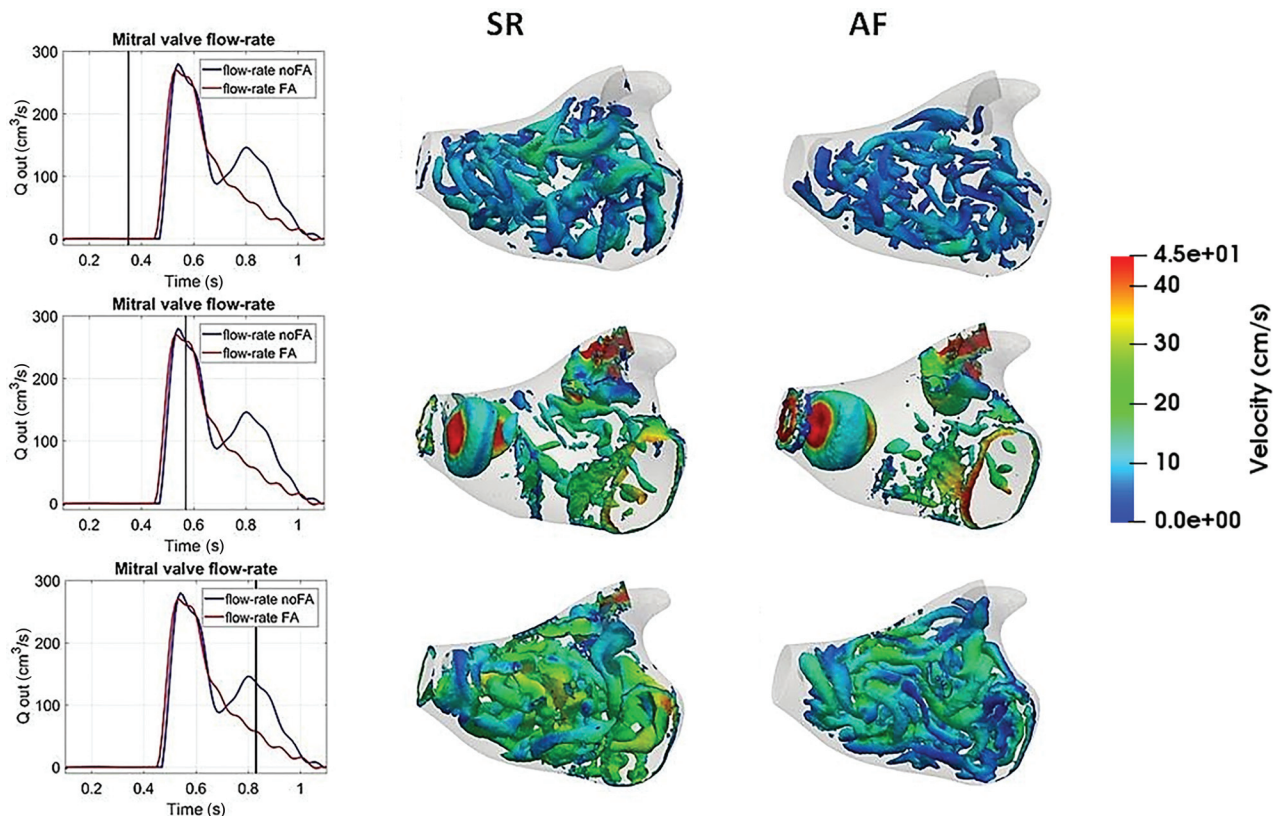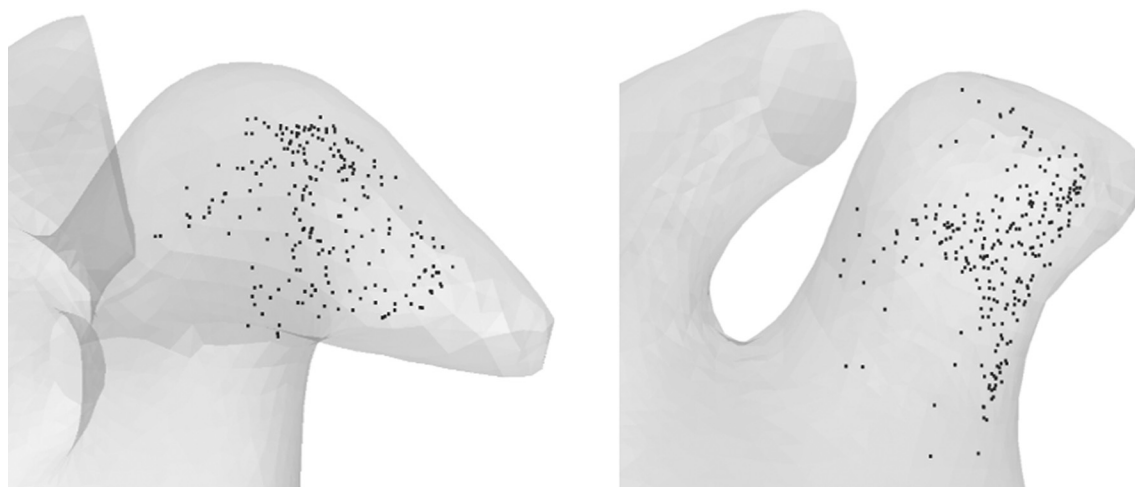

Fig. 9   Visualization of the vortexes structures within the LA for patient 2, at three instants of the cardiac cycle

VELOCITY

VORTICITY
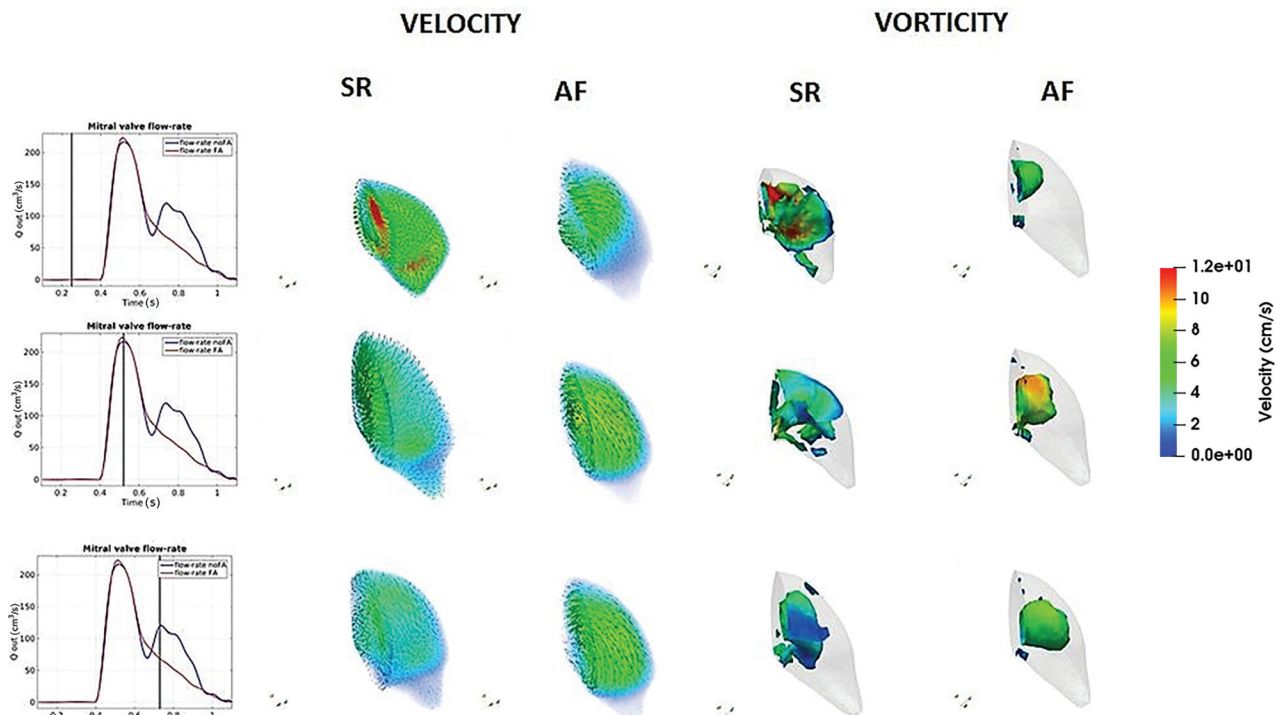
Fig. 10 Visualization of the velocity and of the vortexes structures within the patient 1 LAA at three instants of the cardiac cycle

Fig. 11 Fluid particles distribution in the LAA after three cardiac cycles for the AF simulation in the first and second analyzed patients (left and right panels, respectively)

Moreover, vorticity annihilation between the vortex patches was another key mechanism for the rapid dissipation of these vortexes. We also observed that most of these vortex structures passed through the MV in the left ventricle. We did not notice appreciable differences between the two simulated conditions; however, it was clear that throughout the cardiac cycle, large vortex structures were generated more frequently in the SR condition than the AF one. Our interpretation was that an AF episode could promote a worse blood flow washout effect in the LA, increasing the risk of the intra-atrial blood flow stasis.

Vorticity and the vortex structures simulated in the patient 2 are reported in Fig. 9. We noticed many similarities in the formation of vortex structures between the two patients including the number of vortex structures which was higher in SR condition than in AF also in this patient. However, it seemed that these structures were more numerous and showed higher velocity values compared to the patient 1.

3.2 Analysis of the Left Atrium Appendage Fluid Dynamics. In Fig. 10, we represented the velocity and the vortex structures within the LAA for one patient in three time instants of the cardiac cycle. During ventricular systole in SR, the mean velocity increased (peak value 12 cm/s) and a significant blood flow passed through the LAA. During AF, we did not appreciate this increase of blood flow within the LAA and velocity remained lower, about 7 cm/s. In ventricular diastole, we noticed that fluid started to exit from the LAA. In fact, in this phase, the MV opened and the blood flow passed rapidly from the LA to the LV. The mean velocity in the LAA seemed to be slightly higher in AF condition than in the

SR one. Moreover, in this phase, the LAA contraction in the SR condition was clearly evident, which promoted an increased release of blood flow rate, compared to the AF condition. Then, during the atrial contraction, blood continued to exit from the LAA in the SR condition while it seemed that in AF simulation the blood remained within the LAA, and the differences in the blood flow patterns were due to the lack of motion of the left atrial appendage owing to the presence of the pathology that may cause blood stasis in the LAA. At these three time instants of the cardiac cycle, we observed that velocity in the distal part of the LAA remained almost null for the AF condition with respect to the SR one: this could imply an increment of the thrombi formation probability in this part of the LAA. To sum up, we observed that the LAA motion throughout the cardiac cycle in the SR condition promoted the release of the blood from the LAA, while in the AF condition the lack of contractile activity of the LAA may promote the blood stasis. Moreover, the mean velocity of the blood flow within the LAA throughout the cardiac cycle seemed slightly larger in the SR condition than in the AF one. Concerning the analysis of the vorticity within the LAA, we noticed from Fig. 10, as in the LA, that the number of vortex structures occurred more frequently in the SR condition than in AF. As explained before in the analysis of the vortex structures in the LA, this phenomenon could promote a worse blood flow washout effect also within the LAA during an AF episode. Finally, to quantify a measure of the blood flow stasis in the LAA, we simulated seven cardiac cycles for both conditions. We populated the LAA with 500 fluid particles at the beginning of the fourth heartbeat and we counted how many particles remained inside the LAA after three cardiac cycles (e.g., end of the simulation). The fluid particles were distributed as a sphere around the center c, which represents the midpoint of the LAA centerline. For patient 1, we found that, after three cardiac cycles, 26% of the particles remained in the LAA in SR condition, while 45.6% remained in the LAA, in AF condition. For patient 2 we found that, after three cardiac cycles, 39% of the particles remained in the LAA in SR, while 50.2% remained in the LAA in AF condition. Figure 11 shows the distribution of the fluid particles in the LAA after three cardiac cycles for the AF simulation in the two analyzed patients. These results confirm that AF may promote blood stasis in LAA. In fact the reduction of atrial contraction in AF could imply an expected reduced washout of the LA, as explained before, and mainly of the LAA, although more acutely for the first patient which, in the long term, might be indicative of the generation of blood clots.

4 Conclusions

In this study, we developed what, to the best of our knowledge, is the most advanced effort toward a fully personalized CFD model of atrial blood flow in AF. Hereto, dynamic imaging data were used to extract the patient-specific detailed anatomy and motion model during SR. Moreover, a realistic MV flowrate profile was used to set inflow and outflow boundary conditions. The designed workflow was tested in two different conditions, SR and AF. Differently from previous works in which LA walls in AF were considered rigid [14,23], in our study LA motion in AF was modeled by applying a random displacement to reproduce a disorganized and unsynchronized contraction. In this preliminary testings, the model highlighted expected differences in velocity and vortex formation in the two conditions and confirmed that AF episodes resulted in a reduced washout of the LAA compared to the SR condition, which may lead to the formation of thrombi.

With respect to the work by Otani et al. [16], we developed an automatic image segmentation algorithm which allowed us to reconstruct the 3D atrial structures also including the anatomy of the LAA and the distal and proximal part of the PVs. Moreover, through the *B*-splines image registration procedure, we reconstructed the displacement field of each component of the LA, including the PVs. However, in our work, we did not consider the anatomical model of the left ventricle. The most important difference between our and Otani' framework consists in the boundary conditions imposition at the PVs and at the MVs. The CFD model in Ref. [16] employed zero-gradient velocity and pressure boundary conditions at the PVs and the MV annulus was treated as a surface boundary condition. In our CFD model, we imposed a Dirichlet boundary condition for each PV considering also the PVs sections move and their area change over the cardiac cycle. The choice to scale the velocity according to PVs sectional area was made because we think it is the most appropriate and suitable for the future developments of the model. Other choices would have allowed to take the patient-specific geometry into account but, in view of a clinical application, it could be easier to pass from PW Doppler velocity measurements to the flowrates with this choice in order to directly apply them to the CFD solver. Regarding the MV, we employed a natural boundary condition with a weakly penalization term of the reverse flow, to avoid instability of the discrete formulation of the problem, eventually caused by the backflows at the MV. Finally, with respect to the work by Otani, we simulated the atrial fluid dynamics in SR and AF to compare the two different conditions and to understand the hemodynamic implications of the AF on the LA, with a detailed analysis of the velocity and vorticity also for the LAA.

Our study has several limitations that we will better address in our future works. First of all the results of the model in the two analyzed patients were not benchmarked against experimental clinical measurements, which were not available. In the future works, we are planning to test the model on patients in which personalized intracardiac Doppler flow measurements are available. The developed approach could be easily extended to patient-specific boundary conditions: in particular, having available the PW Doppler measurements from intracardiac echocardiography at the MV and PVs, the flowrates for the CFD model boundary conditions imposition can be directly computed for each patient. Also, the temporal and spatial resolution employed in this work might be insufficient to capture all the turbulent-like flow features. Further investigations on the correlation between the spatial and temporal resolution and the fluid-dynamics parameters to be used in a clinical setting are required in order to evaluate the impact of these numerical variables on the LA hemodynamics. Moreover, the motion field used for AF simulation was based on a modeling approach. New strategies for AF wall motion simulations may include a Fluid Structure Interaction model in which the control of the motion of the computational domain throughout the cardiac cycle could be more realistic than using a random displacement function as the one employed in this study.

Blood flow dynamics obtained in a healthy LA is missing and a comparison with respect to the simulated blood dynamics in SR/AF in a persistent AF LA may provide a better understanding of the hemodynamic implications of AF. We plan to apply the developed pipeline to a larger number of AF subjects, presenting a different range of atrial morphology and function. In particular, we will focus on the different anatomic types of the LAA in order to understand their impact on blood flow stasis.

We believe that the proposed computational framework is feasible and able to successfully compute LA blood flow dynamics in AF. Indeed, after a comprehensive validation, it could represent a significant advancement toward an optimized stroke risk stratification and therapy delivery on a patient-specific basis.

References

[1] Chugh, S. S., Blackshear, J. L., Shen, W.-K., Hammill, S. C., and Gersh, B. J., 2001, "Epidemiology and Natural History of Atrial Fibrillation: Clinical Implications," J. Am. Coll. Cardiol., **37**(2), pp. 371–378.

[2] Go, A. S., Hylek, E. M., Phillips, K. A., Chang, Y., Henault, L. E., Selby, J. V., and Singer, D. E., 2001, "Prevalence of Diagnosed Atrial Fibrillation in Adults: National Implications for Rhythm Management and Stroke Prevention: The Anticoagulation and Risk Factors in Atrial Fibrillation (ATRIA) Study," JAMA, **285**(18), pp. 2370–2375.

[3] Wolf, P. A., Abbott, R. D., and Kannel, W. B., 1991, "Atrial Fibrillation as an Independent Risk Factor for Stroke: The Framingham Study," Stroke, **22**(8), pp. 983–988.

[4] Camm, A. J., Kirchhof, P., Lip, G. Y., Schotten, U., Savelieva, I., Ernst, S., Van Gelder, I. C., Al-Attar, N., Hindricks, G., Prendergast, B., Al-Attar, N., Hindricks, G., Prendergast, B., Heidbuchel, H., Alfieri, O., Angelini, A., Atar, A., D. A., Colonna, P., De Caterina, R., De Sutter, J., Goette, A., Gorenek, B., Heldal, M., Hohloser, S. H., Kolh, P., Le Heuzey, J. Y., Ponikowski, P., and Rutten, F. H., 2010, "Guidelines for the Management of Atrial Fibrillation," Eur. Heart J., **31**(19), pp. 2369–2429.

[5] Fluckiger, J. U., Goldberger, J. J., Lee, D. C., Ng, J., Lee, R., Goyal, A., and Markl, M., 2013, "Left Atrial Flow Velocity Distribution and Flow Coherence Using Four-Dimensional Flow MRI: A Pilot Study Investigating the Impact of Age and Pre-and Postintervention Atrial Fibrillation on Atrial Hemodynamics," J. Magn. Reson. Imaging, **38**(3), pp. 580–587.

[6] Allessie, M., Ausma, J., and Schotten, U., 2002, "Electrical, Contractile and Structural Remodeling During Atrial Fibrillation," Cardiovasc. Res., **54**(2), pp. 230–246.

[7] Gupta, D. K., Shah, A. M., Giugliano, R. P., Ruff, C. T., Antman, E. M., Grip, L. T., Deenadayalu, N., Hoffman, E., Patel, I., Shi, M., Mercuri, M., Mitrovic, V., Braunwald, E., and Solomon, S. D., 2014, "Left Atrial Structure and Function in Atrial Fibrillation: Engage AF-TIMI 48," Eur. Heart J., **35**(22), pp. 1457–1465.

[8] Di Biase, L., Santangeli, P., Anselmino, M., Mohanty, P., Salvetti, I., Gili, S., Horton, R., Sanchez, J. E., Bai, R., Mohanty, S., Pump, A., Cereceda Brantes, M., Gallinghouse, G. J., Burkhardt, J. D., Cesarani, F., Scaglione, M., Natale, A., and Gaita, F., 2012, "Does the Left Atrial Appendage Morphology Correlate With the Risk of Stroke in Patients With Atrial Fibrillation?: Results From a Multicenter Study," J. Am. Coll. Cardiol., **60**(6), pp. 531–538.

[9] Chnafa, C., Mendez, S., and Nicoud, F., 2014, "Image-Based Large-Eddy Simulation in a Realistic Left Heart," Comput. Fluids, **94**, pp. 173–187.

[10] Tagliabue, A., Dedè, L., and Quarteroni, A., 2017, "Complex Blood Flow Patterns in an Idealized Left Ventricle: A Numerical Study," Chaos: An Interdiscip. J. Nonlinear Sci., **27**(9), p. 093939.

[11] Tagliabue, A., Dedè, L., and Quarteroni, A., 2017, "Fluid Dynamics of an Idealized Left Ventricle: The Extended Nitsche's Method for the Treatment of Heart Valves as Mixed Time Varying Boundary Conditions," Int. J. Numer. Methods Fluids, **85**(3), pp. 135–164.

[12] Zhang, L. T., and Gay, M., 2008, "Characterizing Left Atrial Appendage Functions in Sinus Rhythm and Atrial Fibrillation Using Computational Models," J. Biomech., **41**(11), pp. 2515–2523.

[13] Koizumi, R., Funamoto, K., Hayase, T., Kanke, Y., Shibata, M., Shiraishi, Y., and Yambe, T., 2015, "Numerical Analysis of Hemodynamic Changes in the Left Atrium Due to Atrial Fibrillation," J. Biomech., **48**(3), pp. 472–478.

[14] García-Isla, G., Olivares, A. L., Silva, E., Nuñez-Garcia, M., Butakoff, C., Sanchez-Quintana, D., G. Morales, H., Freixa, X., Noailly, J., De Potter, T., and Camara, O., 2018, "Sensitivity Analysis of Geometrical Parameters to Study Haemodynamics and Thrombus Formation in the Left Atrial Appendage," Int. J. Numer. Methods Biomed. Eng., **34**(8), p. e3100.

[15] Menghini, F., Dedè, L., Forti, D., and Quarteroni, A., 2017, "Hemodynamics in a Left Atrium Based on a Variational Multiscale–LES Numerical Model," Politecnico di Milano, Milan, Italy, MOX Report No. 47/2017.

[16] Otani, T., Al-Issa, A., Pourmorteza, A., McVeigh, E. R., Wada, S., and Ashikaga, H., 2016, "A Computational Framework for Personalized Blood Flow Analysis in the Human Left Atrium," Ann. Biomed. Eng., **44**(11), pp. 3284–3294.

[17] Masci, A., Alessandrini, M., Forti, D., Menghini, F., Dedé, L., Tommasi, C., Quarteroni, A., and Corsi, C., 2017, "A Patient-Specific Computational Fluid Dynamics Model of the Left Atrium in Atrial Fibrillation: Development and Initial Evaluation," International Conference on Functional Imaging and Modeling of the Heart, Toronto, Canada, pp. 392–400.

[18] The Task Force for the Management of Atrial Fibrillation of the European Society of Cardiology, 2016, "Guidelines for the Management of Atrial Fibrillation Developed in Collaboration With EACTS," Europace, **18**, pp. 1609–1678.

[19] MATLAB, 1998, "Guide, MATLAB User's," The Mathworks, Natick, MA.

[20] Cignoni, P., Corsini, M., and Ranzuglia, G., 2008, "Meshlab: An Open-Source 3D Mesh Processing System," Ercim News, **73**(45–46), p. 6.

[21] Antiga, L., and Steinman, D. A., 2012, "VMTK: Vascular Modeling Toolkit," .

[22] Unser, M., 1999, "Splines: A Perfect Fit for Signal and Image Processing," IEEE Signal Process. Mag., **16**(6), pp. 22–38.

[23] Sanatkhani, S., and Menon, P. G., 2017, "Relating Atrial Appendage Flow Stasis Risk From Computational Fluid Dynamics to Imaging Based Appearance Paradigms for Cardioembolic Risk," *Imaging for Patient-Customized Simulations and Systems for Point-of-Care Ultrasound*, Springer, Berlin, pp. 86–93.

[24] Khurram, R. A., and Masud, A., 2006, "A Multiscale/Stabilized Formulation of the Incompressible Navier–Stokes Equations for Moving Boundary Flows and Fluid–Structure Interaction," Comput. Mech., **38**(4–5), pp. 403–416.

[25] Donea, J., Huerta, A., Ponthot, J.-P., and Rodriguez-Ferran, A., 2004, "Chapter 14: Arbitrary Lagrangian-Eulerian Methods," *Encyclopedia of Computational Mechanics: Fundamentals*, Vol. 1.

[26] Quarteroni, A., 2010, *Numerical Models for Differential Problems*, Vol. 2, Springer Science & Business Media, Berlin.

[27] Forti, D., and Dedè, L., 2015, "Semi-Implicit BDF Time Discretization of the Navier–Stokes Equations With VMS-LES Modeling in a High Performance Computing Framework," Comput. Fluids, **117**, pp. 168–182.

[28] Nobile, F., 2001, "Numerical Approximation of Fluid-Structure Interaction Problems With Application to Haemodynamics," Ph.D. thesis, EPFL, Lausanne, Switzerland.

[29] Scovazzi, G., 2007, "A Discourse on Galilean Invariance, SUPG Stabilization, and the Variational Multiscale Framework," Comput. Methods Appl. Mech. Eng., **196**(4–6), pp. 1108–1132.

[30] Mansour, M., Holmvang, G., Sosnovik, D., Migrino, R., Abbara, S., Ruskin, J., and Keane, D., 2004, "Assessment of Pulmonary Vein Anatomic Variability by Magnetic Resonance Imaging: Implications for Catheter Ablation Techniques for Atrial Fibrillation," J. Cardiovasc. Electrophysiol., **15**(4), pp. 387–393.

[31] Bazilevs, Y., Gohean, J., Hughes, T., Moser, R., and Zhang, Y., 2009, "Patient-Specific Isogeometric Fluid–Structure Interaction Analysis of Thoracic Aortic Blood Flow Due to Implantation of the Jarvik 2000 Left Ventricular Assist Device," Comput. Methods Appl. Mech. Eng., **198**(45–46), pp. 3534–3550.

[32] Malossi, C., and Deparis, S., 2009, "Lifev Development Guidelines," .

[33] Roelandt, J., and Pozzoli, M., 2001, "On-Invasive Assessment of Left Ventricular Diastolic (Dys) Function and Filling Pressure," Thoraxcentre J., **13**(2), pp. 30–37.